Archives of Civil and Mechanical Engineering (2021) 21:46
https://doi.org/10.1007/s43452-021-00191-w

ORIGINAL ARTICLE

Rapid uniaxial compressive strength assessment by microstructural properties using X-ray CT imaging and virtual experiments

Zhi Zhao[1] · Xiao-Ping Zhou[1]

Received: 8 September 2020 / Revised: 17 January 2021 / Accepted: 1 February 2021 / Published online: 8 March 2021

Abstract

Understanding the mechanical properties plays pivotal roles in rock engineering. This work aims to establish novel relations linking the porosity, ultrasonic wave and fluid saturation to estimate the uniaxial compressive strength (UCS) fast and simply. The uniaxial compressive coupled with ultrasonic wave tests on sandstone samples are carried out to obtain the datasets of the UCS, P-wave and S-wave velocities. X-ray CT imaging technique is employed to capture the microstructure information. The color difference phase separation approach to segment the pore, water and solid phases is proposed, and pore-scale variables to describe the microstructure characteristics are defined. Novel relations to determine the micro velocities of P-wave and S-wave are established, and the modulus of deformation and the physical properties of rocks are evaluated. Novel relation to determine the UCS is established and validated by the real and virtual experiment datasets. Results show that the UCS, P-wave and S-wave velocities computed by the proposed method decrease with increasing fluid saturation. The errors between the calculated and experimental UCS, P-wave and S-wave velocities are all < 5%, showing excellent consistency with each other. The proposed method is effective to estimate the mechanical properties fast and accurately, simplifying the estimation of the UCS in rock engineering.

Keywords Uniaxial compressive strength · Microstructural properties · X-ray CT test · Pore-scale variables · Virtual experiments

Abbreviations

I_{DG}	X-ray CT image
N	Dimension
H_{DG}	Histogram
GI_{RGB}	Color pixel
GI_{ini}	Initial peak threshold
GI_{fin}	Final peak threshold
T_{CDG}	Color difference threshold
ψ_{ave}	Average function
$f_b(x, y)$	Binary pixel
I_{3D}	3D microstructures
$<R_P>$	Pore radius
DPI	Voxel resolution
V_S	S-wave velocity
G	Shear modulus
υ	Poisson's ratio
k_G	Solid phase conductivity
k_P	Pore phase conductivity
$f(x, y)$	Discrete pixel
GI	Gray intensity
I_{CDG}	Color difference image
Γ_{RGB}	Three channel transformation function
Γ_R	Red channel transformation function
Γ_G	Green channel transformation function
Γ_B	Blue channel transformation function
T_B	Pore–solid phase separation threshold
I_{2D}	2D microstructures
φ	Porosity
$<R_G>$	Grain radius
V_P	P-wave velocity
ρ	Density
E_{Ym}	Young modulus
k_{Geo}	Effective thermal conductivity
UCS	Uniaxial compressive strength

✉ Xiao-Ping Zhou
xiao_ping_zhou@126.com

[1] School of Civil Engineering, Wuhan University, Wuhan 430072, China

1 Introduction

Uniaxial compressive strength (UCS) plays pivotal roles in the characterization of the strength properties in rock engineering such as the tunnel excavation [1, 2], the shale–oil–gas exploration [3, 4] and the mineral resource mining [5, 6]. Recently, various methods are employed to determine the uniaxial compressive strength (UCS) of rocks, which are classified into three classifications including the standardized test methods [7, 8], experimental methods [9, 10] and empirical formula methods [11, 12]. For the standard methods, although they are relatively simple, their performances are time-consuming, expensive and tedious owing to the well preparation of the rock core samples. Regarding the experimental methods, there are similar limitations to the Standardized test methods, and there exist some limitations to the accidental error and artificial errors during the experiments. With respect to the empirical formula methods, they are the most common approach to estimate uniaxial compression strength of rocks. Moreover, the previous works [12–14] have verified that there exist excellent relations between uniaxial compressive strength and the P-wave velocity. In addition, there is good relation between the P-wave velocity and the porosity. For instances, Tuğrul and Zarif [13] established the relation between the UCS and the P-wave velocity based on the experimental data of numerous granite samples using the correlation analysis and simple regression analysis methods. Horsrud [15] provided empirical correlations to predict the mechanical properties of shale based on the experimental porosity and the acoustic P-wave velocity of shale cores. Azimian and Ajalloeian [16] proposed the linear relation between the laboratory uniaxial compressive strength and the P-wave velocity of marble samples with a correlation coefficient of 0.91. However, although excellent relations to determine uniaxial compressive strength are provided by the previous works, there inevitably exist some limitations due to the single rock types and the processes to obtain the basic petrophysical properties are tedious and complex. In addition, the relations determining the UCS are nearly all established only either based on the P-wave velocity or porosity. Nevertheless, the effect of the S-wave velocity, fluid saturation on uniaxial compressive strength is not analyzed.

Recently, X-ray CT imaging techniques, owning to the advantages of the non-destructive testing, visual three-dimensional (3D) descriptions of interior microstructures, real-time monitoring, provide effective tools to study the cracking characteristics [17, 18], to predict the permeability by pore-scale characteristics [19, 20] and to investigate the transport characteristics at micro-scale [21, 22]. For examples, Mukunoki et al. [23] studied the cracking evolution of the clay specimen subjected to the bending test using the X-ray CT imaging techniques, in which the cracking characteristics and the deformation fields of the specimens are observed and analyzed detailedly. Yu et al. [24] investigated the effect of pore size, distribution and specific surface on the permeability of the pervious concrete, and the results showed that the permeability increases with increasing pore size, and is the most sensitive to the content of small pores. Liu and Mostaghimi [25] simulated the fluid flow, solute transport and chemical reactions based on the X-ray CT imaging techniques and the Lattice Boltzmann methods, in which the changes of the mechanical properties in porous media during the reactive flow are analyzed. In total, the previous works validated that X-ray CT imaging techniques are excellent tools to understand the cracking, hydraulic and transport properties. Nevertheless, the X-ray CT images are rarely applied to investigate the strength characteristics of geomaterials based on their microstructures.

Therefore, the primary objective of this work is to establish novel relations to predict uniaxial compressive strength more simply and rapidly based on the microstructures of rocks and X-ray CT imaging techniques. Thus, the color difference phase separation method is proposed to reliably segment the pore, water and solid phases. Moreover, the pore-scale variables are defined to obtain the microstructure information. In addition, the novel relations are established to predict the P-wave velocity, S-wave velocity and the UCS. The main advantages of this work, compared with the previous work, are (1) the accurate segmentation with pore, water and solid phases avoiding overestimation or underestimation of pore phase; (2) the quantitative descriptions of the microstructures by the defined pore-scale variables; (3) the better prediction of the P-wave and S-wave characteristics of rocks; and (4) more rapid and simpler determination of the mechanical properties such as the modulus of deformation and UCS.

2 Material and experiment setups

Sandstone is one of the most popular porous geomaterials involving in rock engineering such as the oil–gas exploration, the geothermal energy exploration and the isolation and storage of carbon dioxide. Therefore, understanding the mechanical and transport properties is of paramount importance. In this work, the Bentheimer, Berea and Leopard sandstones are collected to establish novel relations to predict the uniaxial compressive strength more efficiently and simply by X-ray CT test and virtual experiments.

2.1 Rock samples description

Bentheimer sandstone (BES) is a kind of homogeneous rock belonging to the late Early Valanginian of the Lower Cretaceous, mainly located in the southwest of the Lower Saxony Basin [26, 27]. The petrophysical assessment suggests that the Bentheimer sandstone is colored in pale yellow to wheat color. Its porosity ranges from 19 to 25%, its permeability varies from 1500 to 3500 mD, and its UCS changes from 24.14 MPa to 56.03 MPa.

Berea sandstone (BS) is a kind of sedimentary rock widely recognized in the petroleum industry, which belongs to the Upper Devonian, mainly locates in the northern Ohio. It is a transversely isotropic rock with predominant sand-sized grains, which primarily consists of quartz [28, 29]. It is a good reservoir rock with the high porosity of 18–25% and the wide permeability of 10–1000 md, and its UCS ranges from 44.83 MPa to 55.17 MPa.

Leopard sandstone (LS) is a kind of inhomogeneous rock belonging to the Paleozoic. It is colored in dark burlywood with black spots [30, 31]. The petrophysical assessment shows that its porosity changes between 15 and 22%, its permeability varies from 1100 to 1300 md and its UCS ranges from 20.69 MPa to 56.21 MPa.

2.2 Experimental setups

For the laboratory tests, the experiment setups are divided into two sections. One is the X-ray CT test and the other is the uniaxial compression test. For the X-ray CT test, samples with the fluid saturation of 2% (dry) marked by BES2 for Bentheimer sandstone; 6% (dry) and 14%, respectively, marked by BS6 and BS14 for Berea sandstone; and 0% (dry), 5%, 45% and 67%, respectively, marked by LS0, LS5, LS45 and LS67 for Leopard sandstone are first prepared. Then, these samples are scanned by the three-super-resolution (3SR) X-ray CT scanner, as shown in Fig. 1a. During the X-ray CT tests, the voxel resolutions are 4.91 μm for BES samples, 4.63 μm for BS samples and 3.48 μm for LS samples.

Regarding the uniaxial compression test, these prepared samples with a standard size (Φ25 mm × 50 mm) are compressed by the rock mechanical testing device (RMT-301) combined with the aid of the data interface for P-wave and S-wave velocities, as shown in Fig. 1b. For the ultrasonic wave system, the driving voltage ranges from − 850 V to − 250 V and the gain scope for the electrical signal amplifier varies from − 20 dB to + 50 dB. Moreover, the measured petrophysical parameters for theses rock samples subjected to the uniaxial compression are listed in Table 1.

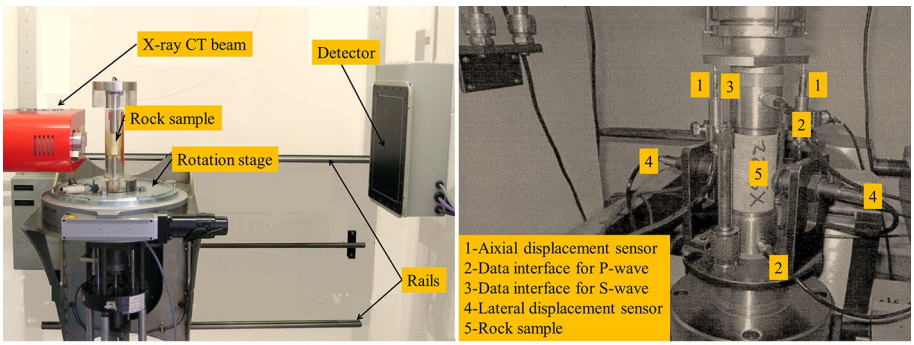

(a) Three super resolution (3SR) X-ray CT apparatus

(b) Rock and concrete mechanical testing apparatus (RMT-301)

Fig. 1 Experiment configurations for (**a**) X-ray CT test and (**b**) uniaxial compression test with P-wave and S-wave

Table 1 Average parameters for different types of sandstone samples

Categories Samples	Density ρ (g/cm^3)	Porosity φ (%)	P-wave velocity V_P (km/s)	S-wave velocity V_S (km/s)	Poisson's ratio ν	Young's modulus E (GPa)	UCS σ (MPa)
BES2	2.3332	22.1491	3.4449	1.8438	0.2992	20.9839	54.5405
BS6	2.3655	18.2266	3.3902	1.8035	0.3027	20.0461	53.9845
BS14	2.3749	16.8683	3.2903	1.6821	0.3106	17.3099	47.8768
LS0	2.3873	15.1461	3.9277	2.1827	0.2766	29.8593	68.0037
LS5	2.3955	14.3475	3.7781	2.0728	0.2846	26.8293	64.7747
LS45	2.4304	10.1810	3. 5657	1.9327	0.2920	23.1235	58.8513
LS67	2.4541	7.5983	3.5173	1.9050	0.2924	22.3940	57.9148

3 Mathematical and virtual models

Constructing the microstructure models of theses sandstone samples plays pivotal roles in fast and simply determining the modulus of deformation and uniaxial compression strength in this work. Therefore, the microstructure models for these samples are first constructed. Then, the pore-scale variables to describe the geometric characteristics of the microstructures are defined. Finally, the mathematical relations to determine the mechanical properties for these virtual models are addressed.

3.1 Microstructure construction

Pore, water and solid phases are the common components in rock mass, and the primary issue to construct the microstructures with geometric characteristics is to accurately capture and extract the component information. X-ray CT imaging techniques are effective to provide the accurate geometric information for real microstructures of different geomaterials. Nevertheless, the separation for the pore, water and solid phases, affecting the rock properties (e.g., porosity, permeability and modulus of deformations), is difficult especially for the three-phase (pore–liquid–solid) geomaterials, which are extremely subjected to overestimation or underestimation of the pore phase by the classical segmentation algorithms such as the OSTU method, watershed segmentation and ISODATA method [32–34]. Therefore, a novel color difference phase separation is proposed to segment the pore, water and solid phases in X-ray CT images of sandstone samples subjected to the interference of fluids in this work. The complete segmentation procedures for the pore, water and solid phase separations are described detailedly as follows.

3.1.1 Procedure one

Histogram estimation. Different structural components in rock mass are usually reflected by different gray intensity values radiographed by the X-ray CT beam, and are presented by different pixel element with different gray intensity values. Thus, the digital phantom image can be written as

$$I_{\mathrm{DG}} = \sum_{x=1}^{N}\sum_{y=1}^{N} f(x,y) = \mathrm{GI}, \quad \mathrm{GI} \in [0,\ 255], \tag{1}$$

where I_{DG} and N represent the X-ray CT image consisting of the discrete pixel $f(x, y)$ with different unique gray intensity value GI and the dimension, respectively.

Moreover, the distribution of these discrete gray intensity values representing the structural components can be drawn by

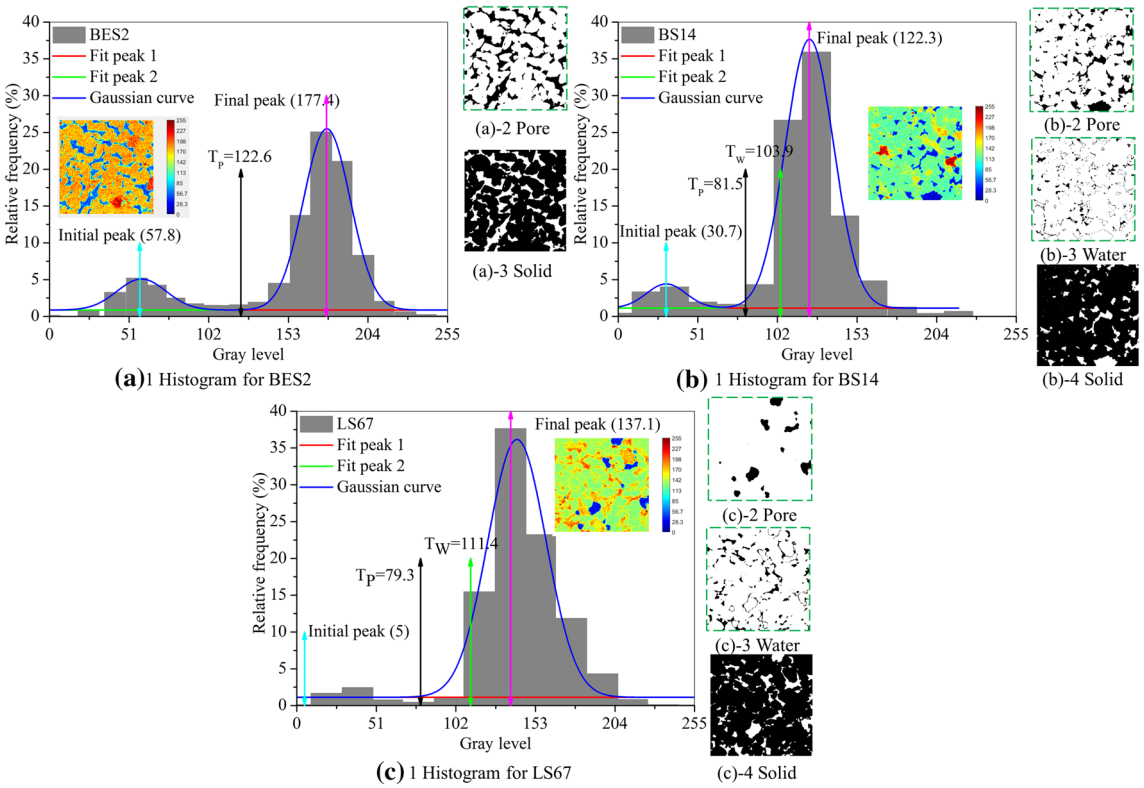

Fig. 2 Sketch maps of procedures to separate the pore, water and solid phases

the histogram of the pixel elements, as shown in Fig. 2a-1–c-1, which can be expressed by

$$H_{\mathrm{DG}} = \int_0^{255} \left(\sum_{x=1}^{N} \sum_{y=1}^{N} f(x,y) = \mathrm{GI} \right) d\mathrm{GI}, \tag{2}$$

where H_{DG} denotes the histogram consisting of different relative frequency of the discrete pixel $f(x, y)$ with unique gray intensity value GI.

3.1.2 Procedure two

Color difference mapping. In fact, some structural components in rock mass have the similar and lower gray intensity values (e.g., the pore boundary and tiny components), which are difficult to recognize, resulting in overestimation or underestimation of different phases. Therefore, the color difference mapping, as shown in Fig. 2a-1–c-1, is applied to highlight these weak components, and can be expressed by

$$\begin{aligned} I_{\mathrm{CDG}} &= \Gamma_{\mathrm{RGB}} \left(\sum_{x=1}^{N} \sum_{y=1}^{N} f(x,y) = \mathrm{GI} \right) = \sum_{x=1}^{N} \sum_{y=1}^{N} \mathrm{GI}_{\mathrm{RGB}} \\ &= \sum_{x=1}^{N} \sum_{y=1}^{N} \begin{cases} \mathrm{GI}_{\mathrm{R}} = \Gamma_{\mathrm{R}}(f(x,y) = \mathrm{GI}) \\ \mathrm{GI}_{\mathrm{G}} = \Gamma_{\mathrm{G}}(f(x,y) = \mathrm{GI}) \\ \mathrm{GI}_{\mathrm{B}} = \Gamma_{\mathrm{B}}(f(x,y) = \mathrm{GI}), \end{cases} \end{aligned} \tag{3}$$

where I_{CDG} denotes the color difference image consisting of the color pixel $\mathrm{GI}_{\mathrm{RGB}}$, Γ_{RGB} is the three channel transformation function consisting of the red, green and blue channel transformation function Γ_{R}, Γ_{G} and Γ_{B}, respectively.

3.1.3 Procedure three

Phase separation threshold estimation. The peak threshold and color difference threshold are calculated to determine the phase separation threshold, respectively. As shown Fig. 2a-1–c-1, the peak thresholds in the initial and final peaks are first computed by determining the extremum, which are expressed as

$$\begin{cases} \frac{\partial H_{\mathrm{DG}}}{\partial f}(f) = 0, \quad f = \mathrm{GI}_{\mathrm{ini}} \; or \; f = \mathrm{GI}_{\mathrm{fin}} \\ \frac{\partial H_{\mathrm{DG}}}{\partial f}\left(\mathrm{GI}_{\mathrm{ini}}^{-}\right) > 0, \quad \frac{\partial H_{\mathrm{DG}}}{\partial f} G\left(I_{\mathrm{ini}}^{+}\right) < 0 \\ \frac{\partial H_{\mathrm{DG}}}{\partial f}\left(\mathrm{GI}_{\mathrm{fin}}^{-}\right) > 0, \quad \frac{\partial H_{\mathrm{DG}}}{\partial f}\left(\mathrm{GI}_{\mathrm{fin}}^{+}\right) < 0, \end{cases} \tag{4}$$

where $\mathrm{GI}_{\mathrm{ini}}$ and $\mathrm{GI}_{\mathrm{fin}}$ are the peak thresholds in the first and final peaks, respectively.

Then, from Fig. 2a-1–c-1, the color difference threshold values are computed by

$$\begin{cases} I_{\mathrm{CDG}}^{i}\left(f_i = \mathrm{GI}_{\mathrm{RGB}}\right) - I_{\mathrm{CDG}}^{i}\left(f_{i+1} = \mathrm{GI}_{\mathrm{RGB}}\right) \neq 0 \\ T_{\mathrm{CDG}}^{j} = \mathrm{GI}_{\mathrm{RGB}}, \;\; j = 1, \; 2 \; \cdots \; M \text{ for different phases}, \end{cases} \tag{5}$$

where $T_{\mathrm{CDG}}^{j=1}$ represents the color difference threshold to segment the pore phase.

Next, the pore phase separation threshold without overestimation or underestimation is determined by

$$T_{\mathrm{P}} = \psi_{\mathrm{ave}}\left(\left(\mathrm{GI}_{\mathrm{ini}} + \mathrm{GI}_{\mathrm{fin}}/2\right), T_{\mathrm{CDG}}^{j=1} \right), \tag{6}$$

where T_{P} is the pore phase separation threshold, ψ_{ave} is the average function.

Finally, repeating Eqs. (3–6), the water phase separation threshold can be also determined in the same way by

$$T_{\mathrm{W}} = \psi_{\mathrm{ave}}\left(\left(\mathrm{GI}_{\mathrm{ini}} + \mathrm{GI}_{\mathrm{fin}}/2\right), T_{\mathrm{CDG}}^{j=2} \right), \tag{7}$$

where T_{W} is the water phase separation threshold, $T_{\mathrm{CDG}}^{j=2}$ is the color difference threshold to segment the water phase.

Totally, using Eqs. (1–7), the pore, water and solid phases in sandstone samples with different water saturation can be segmented accurately, as shown in Fig. 2a-2–c-2, a-3–c-3, b-4–c-4.

3.2 Virtual pore–water–solid phase representation

Once the separation threshold to segment the pore, water and solid phases is determined, the pore, water and solid phases can, respectively, be written as

$$\begin{cases} f_{\mathrm{b}}(x,y) = 0, & f(x,y) \le T_{\mathrm{P}} \\ f_{\mathrm{b}}(x,y) = 1, & T_{\mathrm{P}} < f(x,y) \le T_{\mathrm{W}} \\ f_{\mathrm{b}}(x,y) = 2, & f(x,y) > T_{\mathrm{W}}, \end{cases} \tag{8}$$

where f_{b} represents the binary pixel with 0 for pore, 1 for water and 2 for solid phases.

Thus, with these labeled pixels for pore, water and solid phases, the microstructures for two-dimensional (2D) and three-dimensional (3D) cases can, respectively, be expressed as

$$I_{2\mathrm{D}} = \int_1^N \int_1^N f_{\mathrm{b}}(x,y) dx dy, \tag{9}$$

$$I_{3\mathrm{D}} = \int_1^N \int_1^N \int_1^N f_{\mathrm{b}}(x,y) dx dy dz, \tag{10}$$

where $I_{2\mathrm{D}}$ and $I_{3\mathrm{D}}$ represent the 2D and 3D microstructures with pore, water and solid phases, respectively.

Figure 3, respectively, shows the reconstructed 3D microstructures for the Bentheimer sandstone sample with the fluid saturation of 2% (BS2); Berea sandstone samples with the fluid saturation of 6% (BS6) and 14% (BS14); and Leopard sandstone samples with the fluid saturation of 5% (LS5), 45% (LS45) and 67% (LS67), in which the pore,

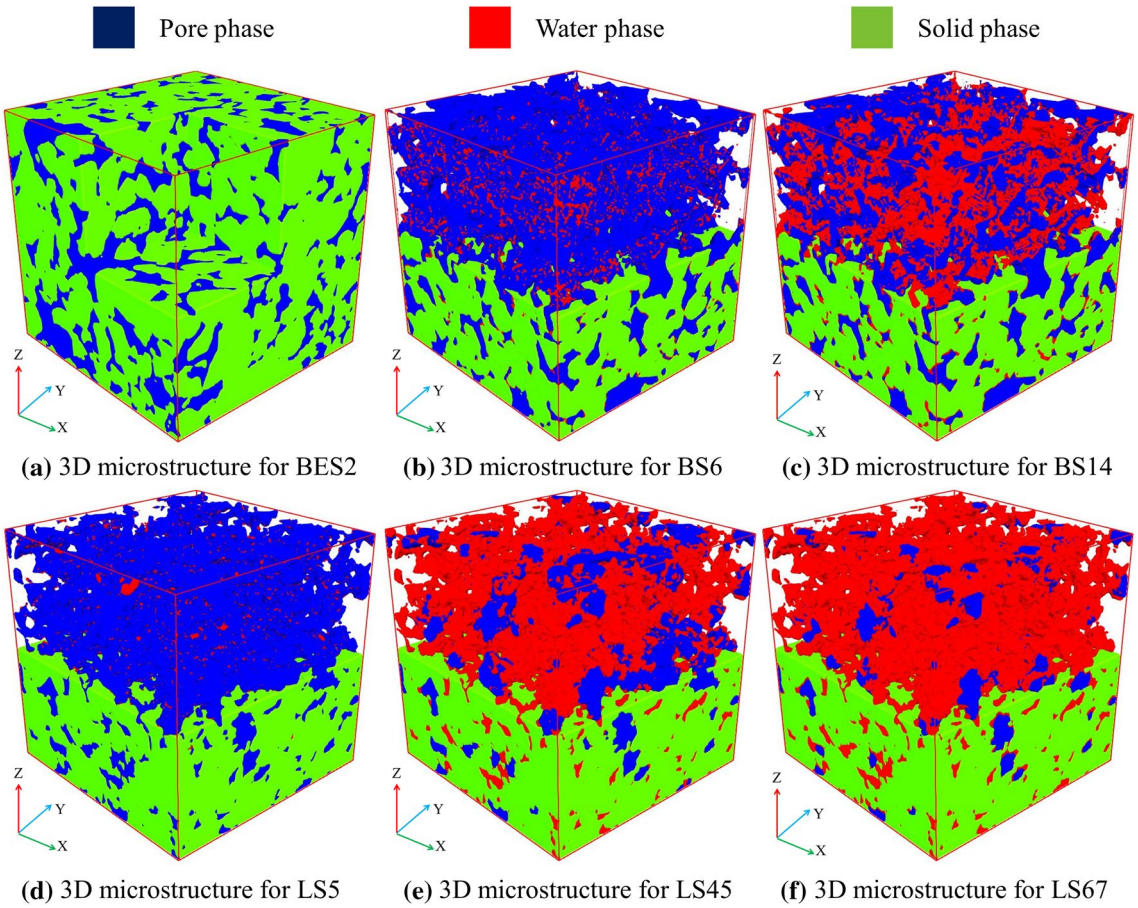

Fig. 3 3D microstructures for different types of sandstone samples with different saturations

water and solid phases are represented by the blue, red and green colors, respectively.

It is easy to find from Fig. 3 that the pore phase decreases with increasing fluid saturation; the pore phases are gradually occupied by water phase due to its flow. For BS2 in Fig. 3a, the pore phase occupies 21.84% of the total volume with water phase of 0.44% and solid phase of 77.72%. Thus, the water phase is almost invisible in its 3D microstructure. For BS6 and BS14, the volume percentage of pore phase decreases from 22.39% to 20.91% with increasing water phase from 1.34% to 3.13%, as shown in Fig. 3b, c. For LS5, LS45 and LS67, the volume percentage of pore phase decreases from 13.97% to 4.18% with increasing water phase from 0.71% to 9.49%, indicating the pore phase is occupied by water phase caused by the water flow along the connective paths in microstructures, as shown in Fig. 3d–f.

3.3 Pore-scale variables definition

Once the pore, water and solid phases are separated by Eq. (1–7), the pore-scale variables can be evaluated based on the microstructural models with pore–water–solid phases. In this work, micro-porosity, pore and grain sizes are defined to establish the novel relationships between the micro-porosity and uniaxial compressive strength, and to investigate their correlations with the pore-scale variables in different types of sandstone with different saturations.

Generally, micro-porosity (φ) is the ratio of the void space to the volume of the porous geomaterials. Thus, the porosity is expressed as

$$\varphi = \frac{\sum_{x=1}^{N}\sum_{y=1}^{N} f_{\mathrm{b}}(x,y) = 0}{\sum_{x=1}^{N}\sum_{y=1}^{N} f_{\mathrm{b}}(x,y) = 0,\ 1,\ 2} \times 100\%. \tag{11}$$

Moreover, the pore size is considered to the equivalent radius of the circle or sphere. Thus, with the marked color pixels for the pore matrixes by Eq. (3), each sub-pore matrix is represented by the different color pixels, and the pore radius can be calculated by

$$\langle R_{\mathrm{P}} \rangle = \left[\mathrm{DPI} * \sum_{i} \left(\sum_{x=1}^{N}\sum_{y=1}^{N} f_{\mathrm{b}}(x,y) = \mathrm{GI}^{i}_{\mathrm{RGB}}\Big|_{f_{\mathrm{b}}(x,y)=0} \right) / \pi \right]^{1/2}, \tag{12}$$

where $\langle R_P \rangle$ denotes the pore radius, DPI is the voxel resolution and GI^i_{RGB} is the color pixels for the i - th pore phase.

Thus, the size for the solid phase (grain size) with the similar approach can also be written as

$$\langle R_G \rangle = \left[\mathrm{DPI} * \sum_i \left(\sum_{x=1}^{N} \sum_{y=1}^{N} f(x,y) = \mathrm{GI}^i_{\mathrm{RGB}} \Big|_{f_b(x,y)=2} \right) / \pi \right]^{1/2}, \tag{13}$$

where $\langle R_G \rangle$ denotes the grain radius.

3.4 Determination of the mechanical properties

Uniaxial compressive strength (UCS) is one of the most mechanical parameters applied in rock engineering [7]. In fact, there exist effective relations between the porosity and the ultrasonic wave velocity. Therefore, efforts are made to establish novel relations to rapidly determine the mechanical properties by X-ray CT imaging techniques.

First, the relations between the micro-porosity and ultrasonic wave velocity extracted from microstructures based on the proposed pore–water–solid phase separation approach and X-ray CT images are established, which are written as.

$$V_P = 4.28208 - 0.04887\varphi \left(R^2 = 0.9666\right), \tag{14}$$

$$V_S = -7.22363 EXP\left(-V_P/5.35265\right) + 5.64403 \left(R^2 = 0.98809\right), \tag{15}$$

where R^2 is the R-Square for the fitted equation, V_P and V_S denote the P-wave and S-wave velocities, respectively.

Then, the relations between the modulus of deformation and the ultrasonic wave velocity can be written as [35–39]

$$\rho = 0.31 \times V_P^{0.25} \tag{16}$$

$$G = \rho V_s^2 / 10^6, \tag{17}$$

$$E_{Ym} = 2G(1 + \nu), \tag{18}$$

$$\nu = (0.5V_P^2, -V_S^2)/(V_P^2, -V_S^2), \tag{19}$$

$$k_{Geo} = (1 - \varphi)k_G + \varphi k_P, \tag{20}$$

where ρ, G, E_{Ym} and ν are, respectively, the density, shear modulus, Young's modulus and Poisson's ratio, and the k_{geo}, k_G and k_p are the effective thermal conductivity, solid phase conductivity and pore phase conductivity, respectively.

The previous works have validated that uniaxial compressive strength (UCS) extremely relates to the P-wave velocity, and linear relations, exponential relations, logarithmic and power relations are established [12, 16]. The main purpose of this work is to develop the simplest relation between UCS and the ultrasonic wave velocity, porosity of sandstone samples with different fluid saturation by X-ray CT imaging techniques. Thus, the mechanical properties including the modulus of deformation and UCS can be rapidly evaluated by the micro-porosity from the microstructures in X-ray CT images of rock samples. The rock properties can be determined by Eqs. (15–19), and UCS can be estimated by

$$\mathrm{UCS} = a + b \times \varphi + c \times V_P + d \times V_s + e \times S, \tag{21}$$

where a, b, c, d and e are the fitting coefficients related to microstructures of rocks, and S is the fluid saturation.

4 Results and discussions

In this work, three samples for each type of sandstone with different fluid saturations (total 21) are prepared and measured to establish the relation between the UCS and P-wave velocity based on the micro-porosity extracted from the microstructures in rocks using X-ray CT imaging. Moreover, the pore-scale variables and variables of mechanical properties are defined, and the effect of the pore-scale variables on the mechanical properties is investigated. In addition, the fitted relations are validated by the virtual and real experimental results.

4.1 Characterization for pore-scale variables

Pore-scale variables offer information enough to quantitatively describe the microstructural characteristics of rocks. Figure 4 shows the porosity, pore and grain size (radius) distributions computed by Eqs. (11–13).

In Fig. 4a, micro-porosities for different samples are 19.096–25.781% with the average of 22.349% for BES2; 12.701–22.764 with the average of 18.227% for BS6; 10.966–20.922% with the average of 16.868% for BS14; 9.338–22.817% with the average of 15.146% for LS0; 9.921–22.992% with the average of 15.147% for LS5; 2.740–18.099% with the average of 9.181% for LS45 and 1.402–13.327% with the average of 6.598% for LS67, respectively. Clearly, micro-porosity decreases with increasing water saturation, suggesting the occupation of microstructural void (pore) phase by water phase.

In Fig. 4b, digital pore sizes (radiuses) for void phases in different samples vary from 30.233 μm to 37.450 μm with the average of 33.678 μm in BES2; from 23.941 μm to 38.708 μm with the average of 31.399 μm in BS6; from 26.020 μm to 36.720 μm with the average of 29.058 μm in BS14; from 15.625 μm to 25.597 μm with the average of 19.832 μm in LS0; from 15.109 μm to 24.678 μm with the average of 19.774 μm in LS5; from 22.895 μm

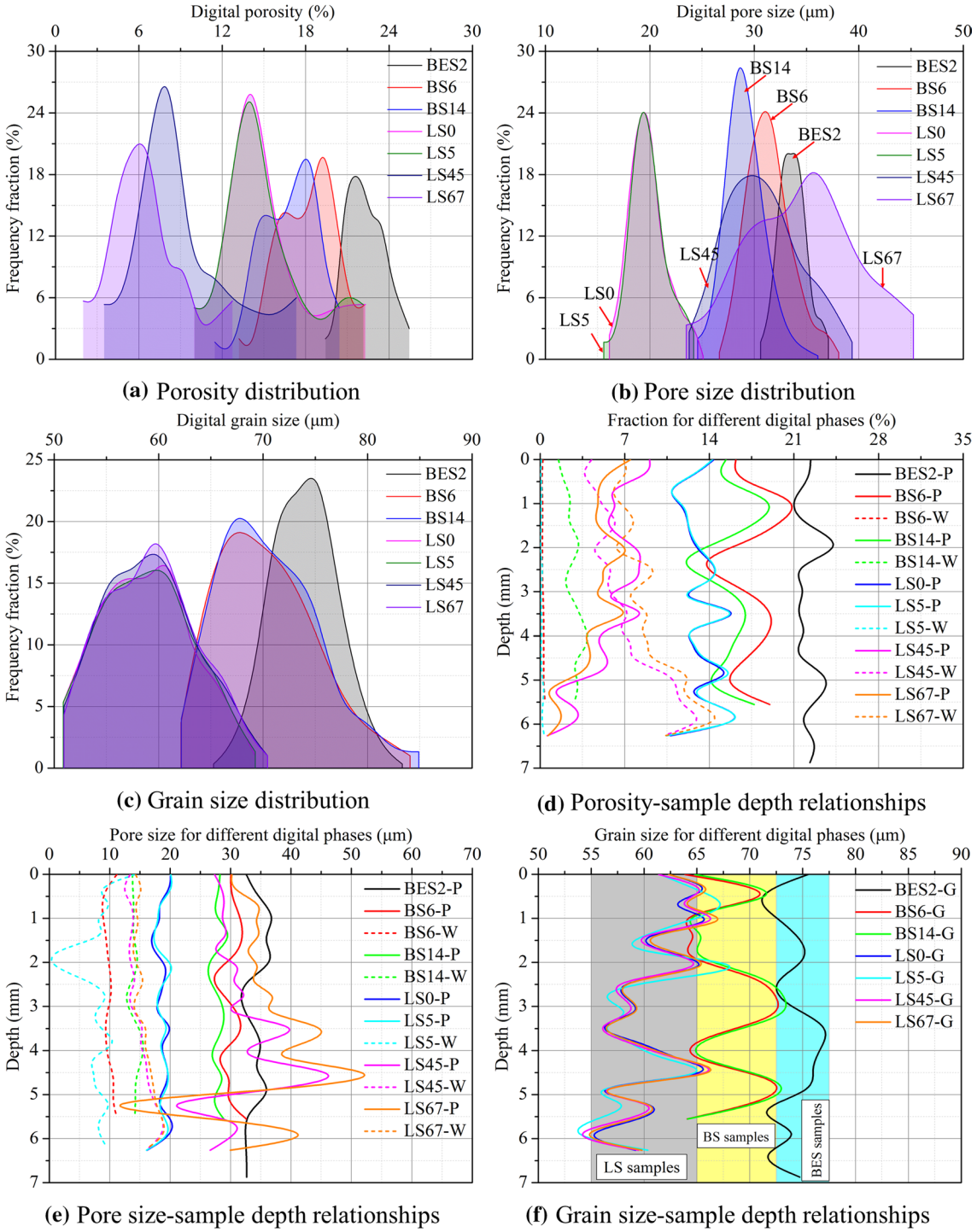

Fig. 4 Pore-scale variables distributions and their relationships with the sampled depth

to 40.234 μm with the average of 30.807 μm in LS45; and from 22.286 μm and 46.438 μm with the average of 34.615 μm in LS67, respectively. Obviously, their minimum and maximum are very close to each other because they are all sandstone rocks with the same geological genesis. However, their distributions have large differences due to the difference of water phase and varied pore structures. Totally, the pore size decreases with increasing fluid saturation. However, the pore size for LS45 and LS67 dramatically increases with increasing water saturation, which may be caused by the deformations of solid and pore skeletons during the large amount of water infiltration.

In Fig. 4c, digital grain sizes for different samples vary between 64.253 μm and 84.333 μm with the average of 73.948 μm for BES2; between 60.923 μm and 85.294 μm with the average of 70.339 μm for BS6; between 60.915 μm and 86.159 μm with the average of 70.431 μm for BS14; between 49.852 μm and 70.272 μm with the average of 58.812 μm for LS0; between 49.851 μm and 70.270 μm with the average of 58.907 μm for LS5; between 49.853 μm and 71.510 μm with the average of 59.056 μm for LS45; and between 49.854 μm and 71.509 μm with the average of 59.138 μm for LS67, respectively. It is easy to find from Fig. 4c that digital grain sizes for the BS and LS samples with different water saturations are very close to each other for BS and LS samples, respectively. Thus, it is easy to conclude that the proposed color difference phase separation approach is accurate to segment the multi-phase microstructures.

Figure 4d–f shows the tendencies of micro-porosity, pore, water and grain phases versus depth of cross sections away from the sample top. In Fig. 4d, as water infiltration increases, the pore phase is occupied gradually by the water phase, the fractions of pore phase decrease and the fractions of water phase increase. Detailedly, the fractions of pore phase and water phase change slightly with the changeable depth in low water saturations. However, the pore phase and water phase change dramatically with high water saturations such as sample LS45 and LS67, in which the water phase is accumulated in the pore phase of microstructures at the bottom of samples. Moreover, the pore size distributions along the depth (Fig. 4e) have the same tendency of those for the fraction of different phases in samples. In addition, the grain size distributions along the depth for each type samples with different water saturations are almost the same, which also implies the accuracy of the proposed method.

Moreover, color cross sections from the same locations (Fig. 5) and different locations in the same sample (Fig. 6) are generated to visually and detailedly declare the change of the porosity, pore size and grain size. It is easy to find form Fig. 5 that the porosity and pore size decrease with increasing fluid saturation, and the pore phase is gradually occupied by the increasing fluid phase. For the pore-scale variables from top to bottom of the same sample in Fig. 6, the porosity first decreases, then increases, and finally decreases with increasing depth of sample, suggesting the

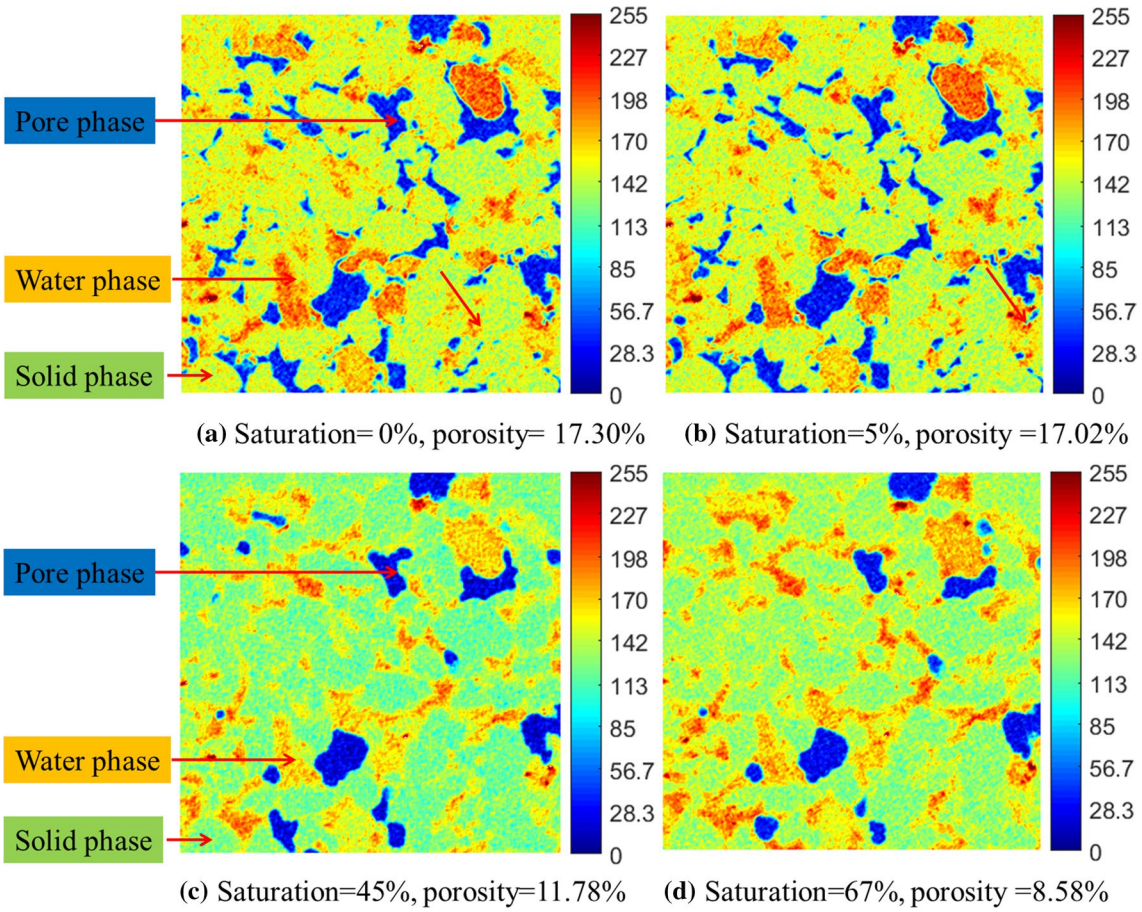

Fig. 5 Cross sections at the height of 0.400 mm for Leopard sandstone samples

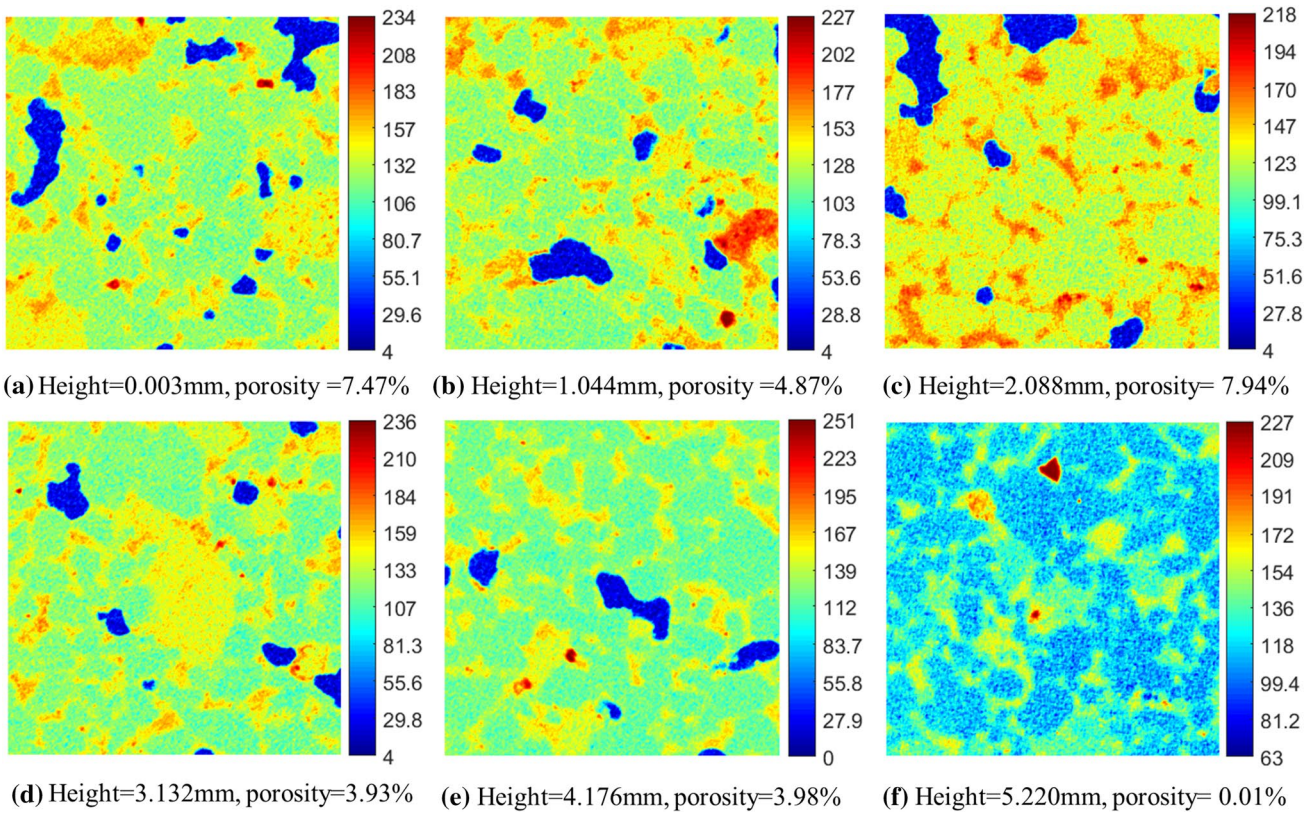

Fig. 6 Cross sections for Leopard sandstone with saturation of 67% at different height

microstructural fluid flow behaviors. First, water phase fills gradually the void (pore) phases, which leads to the decrease of the porosity, as shown in Fig. 6b. Then, the void phases are continually filled with water infiltration, which are not enough to infiltrate along the connective hydraulic path. Thus, the porosity in the next cross section increases temporally, as shown in Fig. 6c. Finally, as the large amount of water infiltration increases, water phase is gradually filled and accumulated in pore phase along the connective hydraulic path. Therefore, the porosity further decreases, as shown in Fig. 6d–e. However, the porosity cannot be zero due to the isolate pore phase or non-connective hydraulic path in microstructures of samples, as shown in Fig. 6f.

4.2 Evaluations for mechanical properties

To validate the accuracy of the predicted rock properties, the density, porosity, Poisson's ratio, and modulus of deformation are computed by Eqs. (14–20) and compared with the experimental results.

Figure 7 shows the errors between the computed and experimental density, porosity, Poisson's ratio and Young's modulus. In Fig. 7a, the density increases as the fluid saturation increases in BES2 to LS67 and the corresponding errors vary from 0 to 0.113% with the average 0.03%. Regarding the porosity, it decreases as the fluid saturation increases in BES2 to LS67 and the corresponding errors vary from 0.127% to 3.672% with the average 1.847%. Referring to the Poisson's ratio, it increases as the fluid saturation increases from BES2 to LS67 and the corresponding errors range from 0.308% to 0.759% with the average 0.507%. With respect to the Young's modulus, it decreases as the fluid saturation increases from BES2 to LS67 and the corresponding errors change from 0.288% to 1.264% with the average 0.582%. In total, all the errors for the density, porosity, Poisson's ratio and Young's modulus are less than 5%, showing good consistency between the experimental data and the computed results by Eqs. (14–20). Therefore, the conclusion can be drawn that the proposed method is effective to evaluate the mechanical properties.

4.3 Virtual experiment verifications

Excepting for the rock properties, the ultrasonic wave velocities and uniaxial compressive strength (UCS) are also investigated and validated by the virtual experiments. Once the basic properties are obtained, the uniaxial compressive and ultrasonic wave tests are carried out using ABAQUS [40], in which the details can be referred to. Considering the virtual uniaxial compression test, the bottom constraint is fixed at

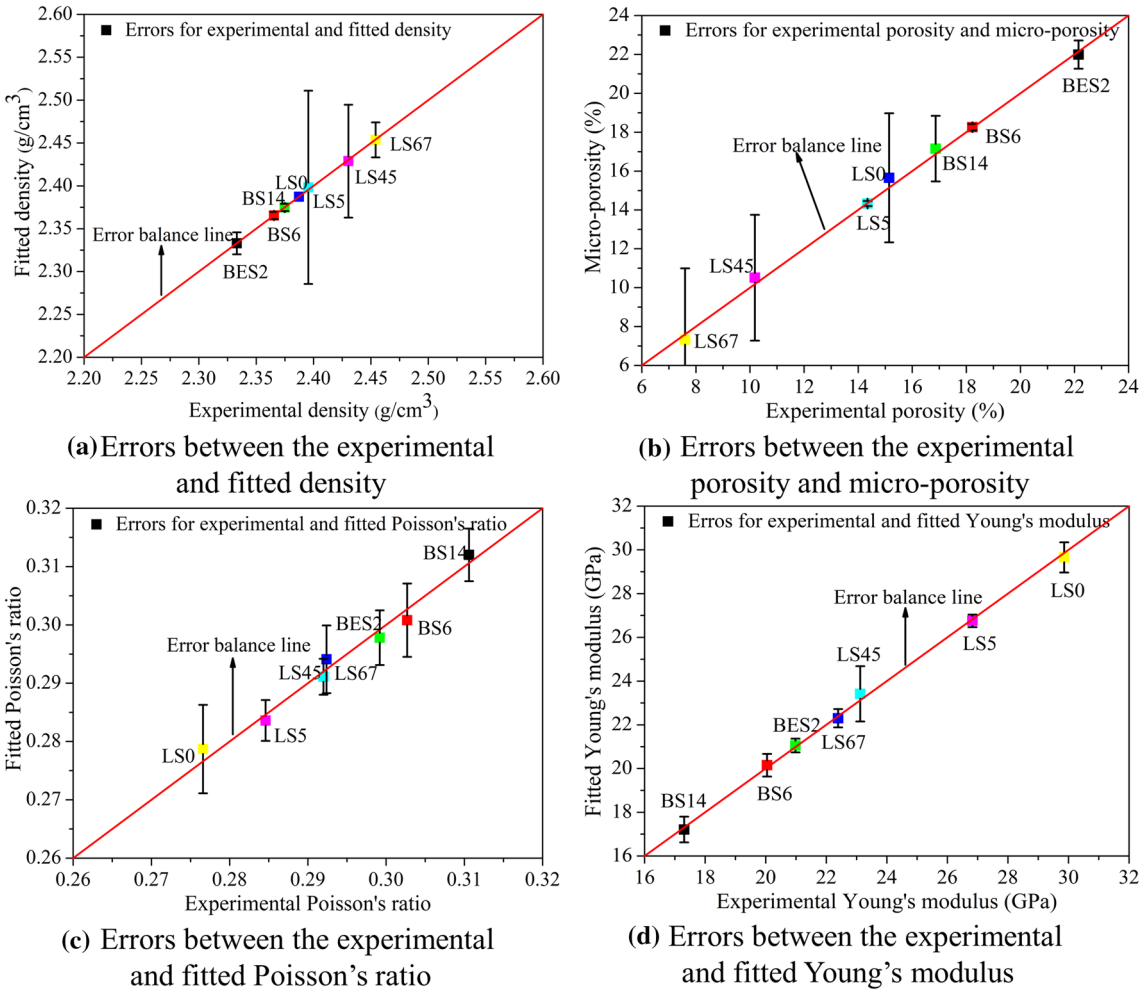

Fig. 7 Errors for the numerical and experimental rock properties

$Y=0$ and the axial loading is considered at the top boundary at $Y=W$, as shown in Fig. 8a. Regarding to the virtual ultrasonic wave test, the bottom is the same as the virtual uniaxial compression test, which is considered to be the fixed constraint boundary and the top is loaded by the wave pressure with the certain frequency, as shown in Fig. 8b.

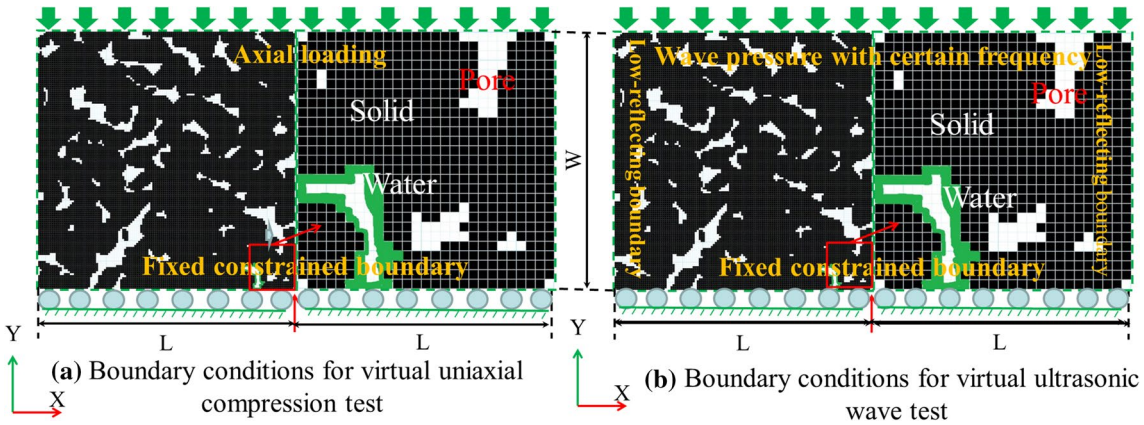

Fig. 8 Sketch maps of boundary conditions for the virtual (**a**) uniaxial compression test and (**b**) ultrasonic wave test

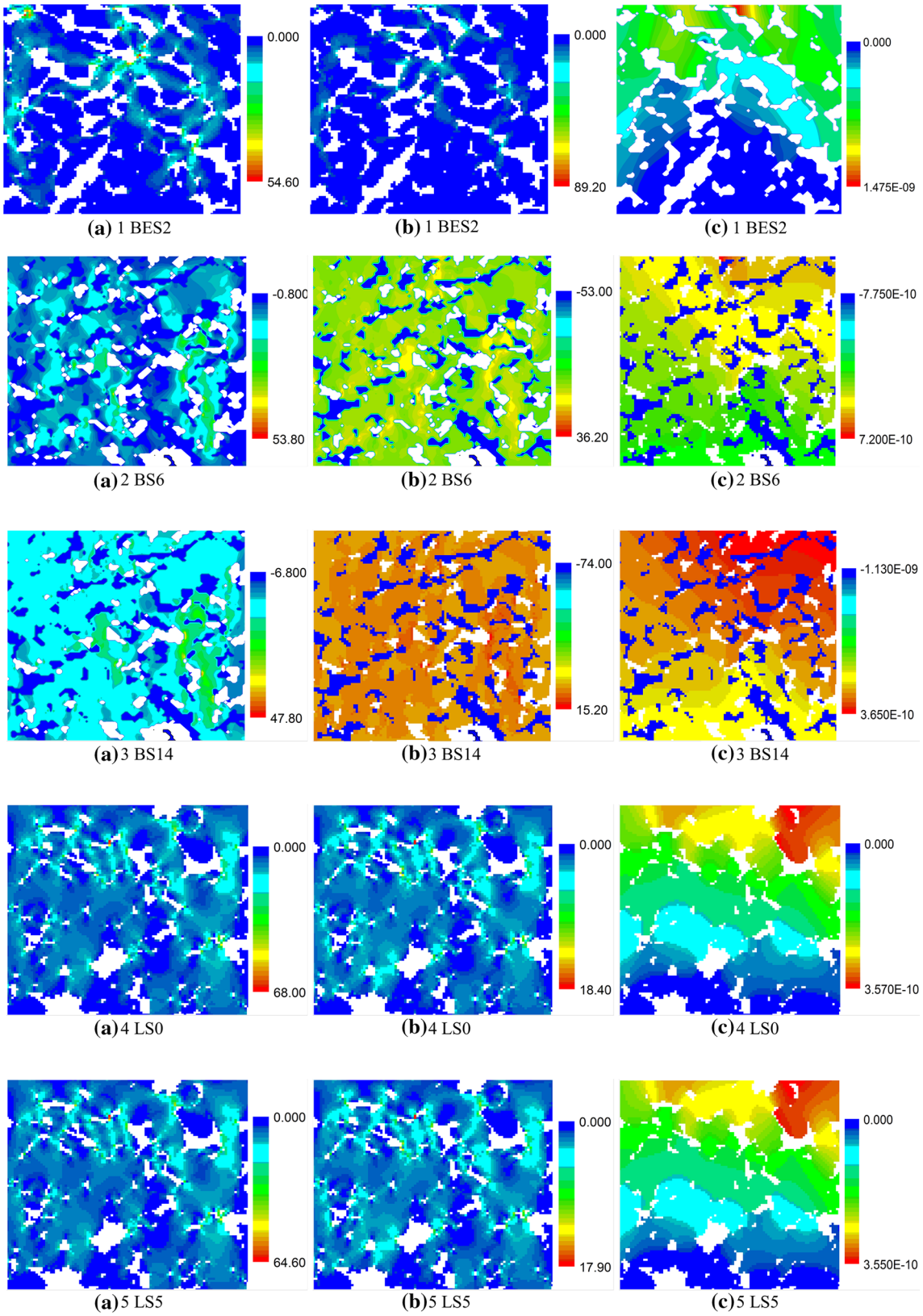

Fig. 9 Cloud maps for (**a**) UCS (MPa) for the virtual uniaxial compression test, and (**b**) the Von-Mises stress (Pa) and (**c**) total displacement (mm) for the ultrasonic wave tests

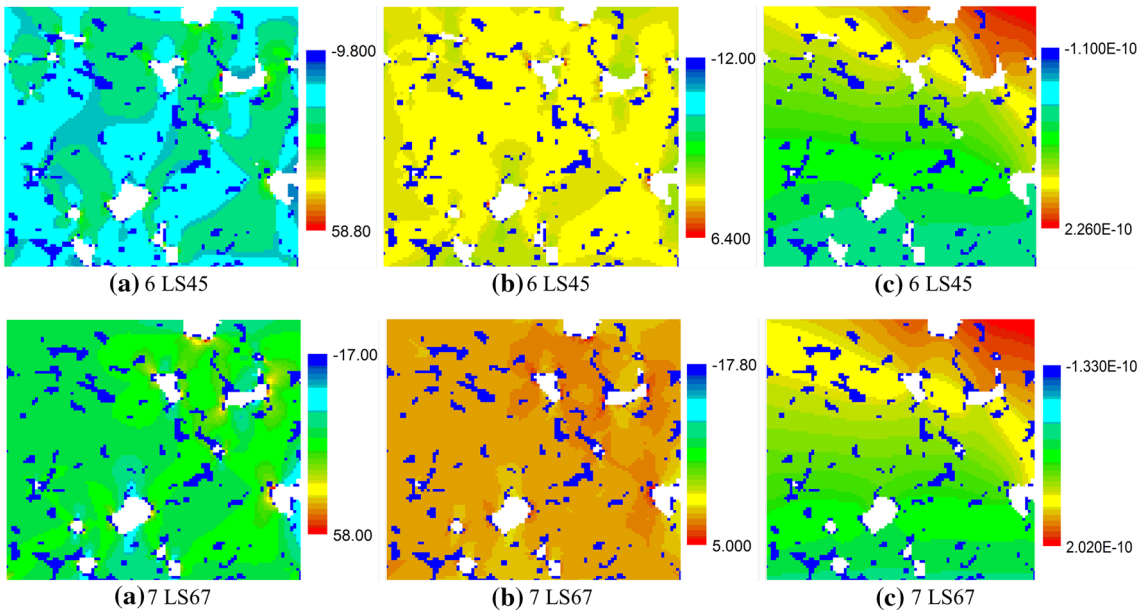

Fig. 9 (continued)

Figure 9 shows the contours of uniaxial compressive strength, Von-Mises stress and total displacement for different types of sandstone samples with different fluid saturations. Uniaxial compressive strength, total displacement and the Von-Mises stress decrease with increasing fluid saturation. Obviously, the water phase plays a negative role for the strength of rock samples. As the water phase gradually fills the pore phase, the local deformation increases, which makes the pore structures change with increasing water content. In addition, the changed pore structure also affects the fluid flow, and the water phase in microstructures makes the contact friction of microstructure decrease. Thus, the strength of rock samples decreases with increasing water phase.

To validate the accuracy and reliability of the proposed method, the P-wave, S-wave velocities and UCS computed by Eqs. (14–21) are compared with the virtual and real experimental datasets. Figure 10a shows the relations between the porosity and P-wave velocity from the experiments in this work and the previous work. Obviously, although the fitted relation between the P-wave velocity and the porosity in this work is below that in the previous work, they agree well with each other. Figure 10b shows the relation between the P-wave and S-wave velocities in this work and the previous work. Moreover, the fitted relation between P-wave and S-wave velocities in this work agrees well with that in the previous work and the fitted relation in this work matches better with the experimental dataset than that in the previous work.

Figure 10c, d show the errors for the P-wave and S-wave velocities from the fitted relation, the virtual and real experiments. For the P-wave velocity, the error between the real experiment and fitted data ranges from 0.001% to 0.451% with the average 0.126%, and the error between the real and virtual experiment data varies from 0.006% to 0.160% with the average 0.074%. For the S-wave velocity, the error between the experiment and fitted data ranges from 0.072% to 0.611% with the average 0.321%, and the error between the real and virtual data varies from 0.124% to 0.262% with the average 0.169%.

Figure 10e, f shows the fitted UCS obtained by Eq. (20) and UCS obtained from the virtual tests and experiments. It is found from Fig. 10e, f that they decrease with increasing fluid saturation in BES2 to LS67. The error between the real experimental UCS and the fitted UCS varies from 0.262% to 0.802% with the average 0.549%, and the error between the real and virtual experimental UCS varies from 0.026% to 1.393% with the average 0.866%. All the errors among the fitted data, the real and virtual experimental data are $< 1.5\%$, implying the accuracy and reliability of the proposed novel relations to determine the mechanical properties. In addition, the residuals for the linear fitting relation to determine uniaxial compressive strength (UCS) fluctuate nearly around 0, showing the accuracy of the proposed relation.

It is easy to conclude from Table 1 and Fig. 10e that the mechanical properties significantly change with increasing water in microstructure. As the water gradually fills the pore space in microstructures, its density increases and the Young's modulus and UCS decreases due to the interaction of water and rocks. The solid skeleton is lubricated,

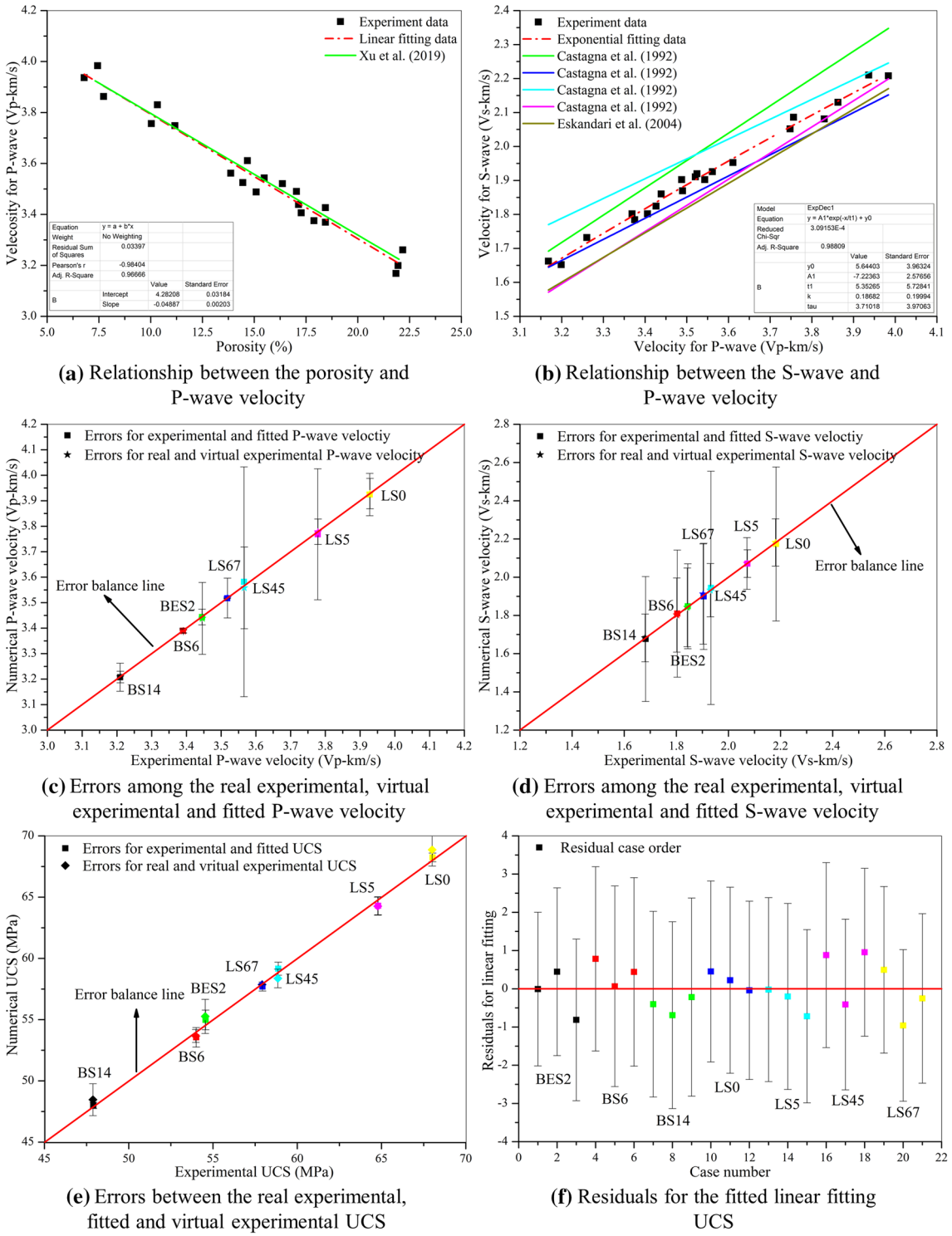

(a) Relationship between the porosity and P-wave velocity

(b) Relationship between the S-wave and P-wave velocity

(c) Errors among the real experimental, virtual experimental and fitted P-wave velocity

(d) Errors among the real experimental, virtual experimental and fitted S-wave velocity

(e) Errors between the real experimental, fitted and virtual experimental UCS

(f) Residuals for the fitted linear fitting UCS

Fig. 10 Errors for the real experimental, fitted and virtual experimental parameters of the ultrasonic wave test and uniaxial compressive test

which makes the contact friction decrease with increasing water phase. Therefore, the rock samples are weakened with increasing water content.

Therefore, the conclusions are drawn that the proposed relations are effective to estimate the rock properties, such as modulus of deformation. In addition, uniaxial compressive strength can be fast and simply estimated by the proposed relation linking to the porosity, ultrasonic wave velocities and fluid saturation with the aid of X-ray CT imaging techniques.

5 Summaries and conclusions

In this work, the novel relations among uniaxial compressive strength and the micro-porosity, ultrasonic wave velocity and fluid saturation have been established to simply evaluate uniaxial compressive strength with the aid of X-ray CT imaging techniques. The color difference phase separation approach has been proposed to accurately segment the pore, water and solid phases, and the pore-scale variables have been defined to describe the microstructural characteristics. The rock properties are computed by the proposed relations and validated by the real and virtual experiments with the microstructural models of rocks. The main conclusions are drawn as follows:

(1) The proposed color difference phase separation approach can segment the pore, water and solid phases without overestimating and underestimating. Thus, the microstructural characteristics of different phases can be well described by the defined pore-scale variables, such as the pore size, which are helpful to understand the effects of pore space on the mechanical properties of rocks
(2) The established novel relation between micro-porosity and P-wave velocity, and relation between the P-wave and S-wave velocities are effective to describe the wave characteristics in rocks, which are helpful to understand the dynamic responses of rock mass under earthquakes.
(3) The proposed novel relation among the UCS and the porosity, P-wave velocity, S-wave velocity and the fluid saturation based on the images improves the efficiency to determine the mechanical properties, such as the modulus of deformation and UCS, which is helpful to evaluate the safety and stability of deep rock engineering.

Author contributions Conceptualization: Zhi Zhao. Methodology: Xiao-Ping Zhou. Writing—original draft preparation: Zhi Zhao, Xiao-Ping Zhou. Funding acquisition: Xiao-Ping Zhou.

Funding The work is supported by the National Natural Science Foundation of China (Nos. 51839009, 52027814, 51679017).

Compliance with ethical standards

Conflict of interest The authors declare no conflict of interest.

Availability of data and material There are no data or materials available for this manuscript.

Code availability There are no codes available for this manuscript.

References

1. Wang S, Li D, Li C, Zhang C, Zhang Y. Thermal radiation characteristics of stress evolution of a circular tunnel excavation under different confining pressures. Tunn Undergr Space Technol. 2018;78:76–83.
2. Liang Z, Gong B, Li W. Instability analysis of a deep tunnel under triaxial loads using a three-dimensional numerical method with strength reduction method. Tunn Undergr Space Technol. 2019;86:51–62.
3. Xiao D, Lu S, Yang J, Zhang L, Li B. Classifying multiscale pores and investigating their relationship with porosity and permeability in tight sandstone gas reservoirs. Energy Fuels. 2017;31(9):9188–200.
4. Ojha SP, Misra S, Tinni A, Sondergeld C, Rai C. Relative permeability estimates for Wolfcamp and Eagle Ford shale samples from oil, gas and condensate windows using adsorption-desorption measurements. Fuel. 2017;208:52–64.
5. Meng Y, Tang L, Yan Y, Oladejo J, Jiang P, Wu T, Pang C. Effects of microwave-enhanced pretreatment on oil shale milling performance. Energy Procedia. 2019;158:1712–7.
6. Zhao Y, Song H, Liu S, Zhang C, Dou L, Cao A. Mechanical anisotropy of coal with considerations of realistic microstructures and external loading directions. Int J Rock Mech Min Sci. 2019;116:111–21.
7. ISRM. Rock characterization testing and monitoring ISRM suggested methods. Oxford: Pergamon Press; 1981.
8. ASTM. Standard test method of unconfined compressive strength of intact rock core specimens. ASTM Standard. 04.08 (D2938). 1986.
9. Farrokhrouz M, Asef MR. Experimental investigation for predicting compressive strength of sandstone. J Nat Gas Sci Eng. 2017;43:222–9.
10. Ashtari M, Mousavi SE, Cheshomi A, Khamechian M. Evaluation of the single compressive strength test in estimating uniaxial compressive and Brazilian tensile strengths and elastic modulus of marlstone. Eng Geol. 2019;248:256–66.
11. Sharma PK, Singh TN. A correlation between P-wave velocity, impact strength index, slake durability index and uniaxial compressive strength. Bull Eng Geol Environ. 2008;67:17–22.
12. Tuğrul A, Zarif IH. Correlation of mineralogical and textural characteristics with engineering properties of selected granitic rocks from Turkey. Eng Geol. 1999;51:303–17.
13. Chang C, Zoback MD, Khaksar A. Empirical relations between rock strength and physical properties in sedimentary rocks. J Petrol Sci Eng. 2006;51(3–4):223–37.
14. Jamshidi A, Zamanian H, Zarei SR. The effect of density and porosity on the correlation between uniaxial compressive strength and P-wave velocity. Rock Mech Rock Eng. 2017;51(4):1279–86.
15. Horsrud P. Estimating mechanical properties of shale from empirical correlations. SPE Drill Complet. 2001;16:68–73.
16. Azimian A, Ajalloeian R. Empirical correlation of physical and mechanical properties of marly rocks with P wave velocity. Arab J Geosci. 2015;8:2069–79.
17. Löffl C, Saage H, Göken M. In situ X-ray tomography investigation of the crack formation in an intermetallic beta-stabilized TiAl-alloy during a stepwise tensile loading. Int J Fatigue. 2019;124:138–48.
18. Zhao Z, Zhou XP. Digital energy grade-based approach for crack path prediction based on 2D X-ray CT images of geomaterials. Fatigue Fract Eng Mater Struct. 2019;42(6):1292–307.

19. Zhao Z, Zhou XP. An integrated method for 3D reconstruction model of porous geomaterials through 2D CT images. Comput Geosci. 2019;123:83–94.
20. Cao Q, Gong Y, Fan T, Wu J. Pore-scale simulations of gas storage in tight sandstone reservoirs for a sequence of increasing injection pressure based on micro-CT. J Nat Gas Sci Eng. 2019;64:15–25.
21. Kato S, Yamaguchi S, Uyama T, Yamada H, Tagawa T, Nagai Y, Tanabe T. Characterization of secondary pores in washcoat layers and their effect on effective gas transport properties. Chem Eng J. 2017;324:370–9.
22. Bashtani F, Taheri S, Kantzas A. Scale up of pore-scale transport properties from micro to macro scale; network modelling approach. J Petrol Sci Eng. 2018;170:541–62.
23. Mukunoki T, Nakano T, Otani J, Gourc JP. Study of cracking process of clay cap barrier in landfill using X-ray CT. Appl Clay Sci. 2014;101:558–66.
24. Yu F, Sun D, Hu M, Wang J. Study on the pores characteristics and permeability simulation of pervious concrete based on 2D/3D CT images. Constr Build Mater. 2019;200:687–702.
25. Liu M, Mostaghimi P. Pore-scale simulation of dissolution-induced variations in rock mechanical properties. Int J Heat Mass Transf. 2017;111:842–51.
26. Kemper E. Geologischer Führer durch die Grafschaft Bentheim und die angrenzenden Gebiete. Verlag Heimatverein der Grafschaft Bentheim, Nordhorn, Germany. 1968.
27. Malmborg P. Correlation between diagenesis and sedimentary facies of the Bentheim Sandstone, the Schoonebeek field. The Netherlands: Dissertations in Geology at Lund University; 2002.
28. Churcher PL, French PR, Shaw JC, Schramm LL. Rock properties of Berea sandstone, Baker dolomite, and Indiana limestone. In: Paper presentated at the SPE International Symposium on Oilfield Chemistry), SPE. 1991; SPE: 431–446.
29. Kim KY, Zhuang L, Yang H, Kim H, Min KB. Strength anisotropy of Berea sandstone: results of X-ray computed tomography, compression tests, and discrete modeling. Rock Mech Rock Eng. 2016;49(4):1201–10.
30. Herring AL, Andersson L, Schlüter S, Sheppard A, Wildenschild D. Efficiently engineering pore-scale processes: force balance and topology during nonwetting phase trapping in porous media. Adv Water Resour. 2015;79:91–102.
31. Liu Z, Herring A, Arns C, Berg S, Armstrong RT. Pore-scale characterization of two-phase flow using integral geometry. Transp Porous Media. 2017;118(1):99–117.
32. Zhao Z, Zhou XP. 3D Digital analysis of cracking behaviors of rocks through 3D reconstruction model under triaxial compression. J Eng Mech. 2020;146(8):04020084.
33. Bieniek A, Moga A. An efficient watershed algorithm based on connected components. Pattern Recogn. 2000;33(6):907–16.
34. Venkateswarlu NB. Raju PSVSK. Fast ISODATA clustering algorithms. Pattern Recogn. 1992;25(3):335–42.
35. Yu C, Ji S, Li Q. Effects of porosity on seismic velocities, elastic moduli and Poisson's ratios of solid materials and rocks. J Rock Mech Geotech Eng. 2016;8(1):35–49.
36. Gardner GHF, Gardner IW, Gregory AR. Formation velocity and density—the diagnostic basics for stratigraphic traps. Geophysics. 1974;39(6):770–80.
37. Boumiz A, Vernet C, Cohen TF. Mechanical properties of cement pastes and mortars at early ages. Adv Cem Based Mater. 1996;3(3):94–106.
38. Palomar I, Barluenga G. Assessment of lime-cement mortar microstructure and properties by P- and S-ultrasonic waves. Constr Build Mater. 2017;139:334–41.
39. Xu Z, Shi W, Zhai G, Clay C, Zhang X, Peng N. A rock physics model for characterizing the total porosity and velocity of shale: a case study in Fuling area. China Mar Petrol Geol. 2019;99:208–26.
40. Simulia DCS. Abaqus. Abaqus/Standard 6.11, User's Manual, Dessault Systems; Abaqus: Providence, RI, USA. 2011